RADIO SCIENCE, VOL. 0, NO. 0, PAGES 1–11, MONTH 2001

Atmospheric radar imaging using multiple-receiver and multiple-frequency techniques

Tian-You Yu[1] and Robert D. Palmer

Department of Electrical Engineering and Center for Electro-Optics, University of Nebraska, Lincoln, Nebraska, USA

Abstract. Atmospheric radar imaging techniques have shown promise in revealing the fine-scale structure of the atmosphere within the resolution volume of the radar. Enhanced resolution can be obtained in both angle and range by using spaced receivers and shifted frequencies, respectively. The distinct techniques have been termed coherent radar imaging (CRI) for angular resolution enhancement and range imaging (RIM) for radial resolution improvement. Because of the mathematical similarities between CRI and RIM it is possible to derive a generalization of both techniques. In this work, the three-dimensional (3-D) imaging technique, which uses multiple receivers and multiple frequencies simultaneously, is developed for the first time. Three-dimensional imaging has the advantage of mitigating the limitations of beam width as well as pulse width of a conventional radar to simultaneously improve both angular and range resolution. It is shown that CRI and RIM are special cases of 3-D imaging. The mathematical problem is formulated as an inverse problem with solutions provided by the Fourier, Capon, and maximum entropy (MaxEnt) methods. These three 3-D imaging methods are verified and statistically tested through numerical simulations.

1. Introduction

Observations of the fine refractivity structure in the atmosphere are fundamentally important for the understanding of small-scale atmospheric processes and associated meteorological events. Therefore both in situ and remote-sensing instruments with better resolution are desirable. For an atmospheric radar, spatial resolution is limited in range and angle by the system bandwidth and beam width, respectively. Although angular and range resolution could be enhanced by means of decreasing the transmitter beam width and pulse length, respectively, neither refinement can be achieved easily or economically. Additionally, a larger transmitter power would be needed to compensate for the reduction in size of the resolution volume. For these reasons, significant effort has been put forth to overcome resolution limitations. For example, many sophisticated techniques have been developed to improve angular resolution based on the interferometry technique [*Pfister*, 1971; *Woodman*, 1971]. The interferometry technique has been implemented using both spatially separated receivers and shifted transmit frequencies. The former technique is termed spatial interferometry with the capability of improving angular resolution [e.g., *Röttger and Vincent*, 1978; *Röttger and Ierkic*, 1985; *Kudeki and Woodman*, 1990; *Palmer et al.*, 1995], and the latter is the so-called frequency domain interferometry (FDI) technique, which can estimate the position and width of a layer within a single range gate [e.g., *Kudeki and Stitt*, 1987; *Franke*, 1990; *Chilson and Schmidt*, 1996].

Atmospheric radar imaging techniques, which include coherent radar imaging (CRI), range imaging (RIM), and three-dimensional (3-D) imaging, are designed to enhance resolution in angle, range, and both angle and range, respectively. Atmospheric radar imaging is an outgrowth of interferometry techniques and is developed in an attempt to reconstruct the atmospheric reflectivity field within the resolution volume using multiple receivers and/or multiple frequencies. Therefore it is possible to study the scattering media in dimensions of angle and/or range independently for each instance in time. Such processing is not possible with conventional radars. Note that the term "3-D imaging" was also used

[1]Now at Atmospheric Technology Division, National Center for Atmospheric Research, Boulder, Colorado, USA.

Paper number 2000RS002622.
0048-6604/01/2000RS002622$11.00

by *Chau and Woodman* [2001], in whose paper the horizontal structure was revealed by CRI and the vertical information was obtained using the typical gating process. However, the term ''3-D imaging'' presented in this study is specifically used for the technique which uses multiple receivers and multiple frequencies to estimate the three-dimensional structure within the radar volume.

Although imaging techniques have been widely used in various fields such as radio astronomy, sonar, and seismic imaging [e.g., *Haykin et al.*, 1985 and references therein], CRI was first introduced into the atmospheric community by *Kudeki and Sürücü* [1991] . By correlating signals from spatially separated receivers the angular distribution of the atmospheric structure was revealed. *Woodman* [1997] has proposed that CRI problems can be postulated as an inverse problem which could be solved by several competing approaches. He pointed out that model-based approaches such as the maximum entropy (MaxEnt) method [*Hysell*, 1996; *Hysell and Woodman*, 1997] can provide less biased estimates than the traditional Fourier method [*Kudeki and Sürücü*, 1991]. *Palmer et al.* [1998] have applied another resolution-enhanced technique, the Capon method [*Capon*, 1969], to the CRI problem. Comparisons of various CRI methods were made by *Yu et al.* [2000], *Chau and Woodman* [2001], and *Hélal et al.* [2001]. Recently, *Palmer et al.* [1999] have developed RIM, which uses a similar concept to CRI but is implemented using a multiple-frequency technique. As a result, the range distribution of the atmospheric structure can be investigated at a fine scale using shifted transmit frequencies without prior assumptions such as the shape of a layer and the number of layers required in FDI techniques. In their paper, the mathematical description of RIM was provided, and the Fourier and Capon methods were implemented using simulated data. A similar approach was proposed by *Luce et al.* [2001] but was termed frequency domain radar interferometric imaging (FII). The MaxEnt RIM implementation, developed by *Yu* [2000], was shown to have similar performance to Capon RIM for high signal-to-noise ratio (SNR). Subsequently, the RIM technique was further justified during a field experiment and was shown to have similarities with in situ measurements by *Chilson et al.* [2001] and *Palmer et al.* [2001]. The 3-D imaging technique, which uses both spaced receivers and shifted frequencies, will be exploited in this work. It has the potential to reveal atmospheric structure with three-dimensional scales much smaller than the resolution volume. The goal of this work is not only to develop a new technique but also to provide a generalized theoretical model of atmospheric radar imaging.

The mathematical basis of atmospheric radar imaging is derived in section 2, where a generalized relationship between the measured visibility and the estimated brightness distribution is established. The theory is generalized to include the existing CRI and RIM techniques, which are shown to be special cases of 3-D imaging. Three estimation methods, the Fourier, Capon, and MaxEnt methods, are studied in section 3 for the case of 3-D imaging. In section 4, numerical simulations are used to study the robustness of these methods.

2. Atmospheric Radar Imaging: Mathematical Formulation

2.1. General Theory: Three-Dimensional Imaging

It was mentioned in section 1 that 3-D imaging is a generalization of CRI and RIM using multiple receivers and multiple frequencies simultaneously. Therefore the analytical form of the correlation function of two signals from spaced receivers and shifted frequencies is necessary. The general geometry of atmospheric radar imaging is given in Figure 1, where a Cartesian coordinate system is used with the positive x, y, and z axes pointing in the east, north, and vertical directions, respectively.

The transmitter is located at the origin, and the position vectors of the ith and jth receivers are denoted by $\mathbf{D}_i$ and $\mathbf{D}_j$, respectively. Usually, the transmitter and receivers are coplanar although the model is completely general. The correlation function between signals from the ith receiver associated with radar wave number of k_m and the jth receiver associated with radar wave number of k_n can be represented in the following form:

$$R(\mathbf{D}_i, k_m, \mathbf{D}_j, k_n, \tau) = \int b(\mathbf{a}, R, f)\, W^2(\mathbf{a}, R) \cdot e^{j2\pi f\tau}\, e^{j\varphi} d\Omega\, dR\, df, \tag{1}$$

$$\varphi = -2\Delta k\, R + k_m \mathbf{a} \cdot \mathbf{l} + \Delta k\, \mathbf{a} \cdot \mathbf{D}_j, \tag{2}$$

where $W(\mathbf{a}, R)$ is the weighting function of the radar system and $b(\mathbf{a}, R, f)$ is termed the ''brightness spectrum,'' which is the power density caused by fluctuations of refractive index as a function of three-dimensional location (represented by range R and angular location $\mathbf{a}$) and Doppler frequency f. A detailed derivation of $R(\mathbf{D}_i, k_m, \mathbf{D}_j, k_n, \tau)$ and the definitions of variables in (1) and (2) are given in Appendix A.

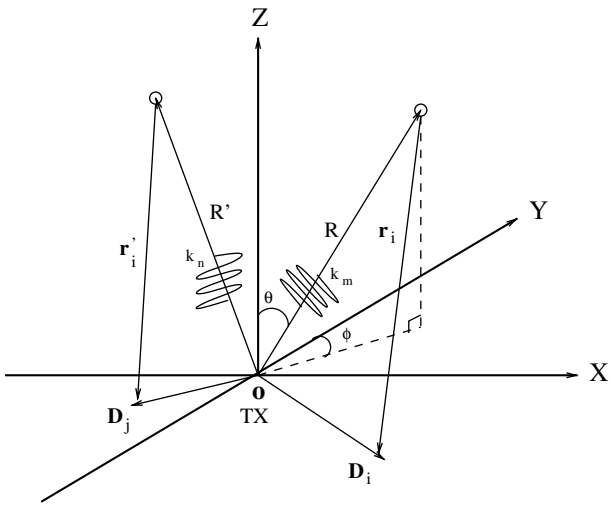

Figure 1. A general configuration of atmospheric radar imaging illustrating signals from spatially separated receivers and shifted transmitted frequencies. The transmitter is located at the origin. A scattering irregularity is located at **R** associated with zenith angle θ and azimuth angle ϕ while the distance from scattering irregularity back to receiver i is denoted by r_i. Signals from receivers located at $\mathbf{D}_i$ and $\mathbf{D}_j$ are associated with radar wave numbers of k_m and k_n, respectively.

A useful and practical relationship can be obtained by calculating the correlation function at zero temporal lag ($\tau = 0$) in (1).

$$R(\mathbf{D}_i, k_m, \mathbf{D}_j, k_n, \tau)|_{\tau=0} = \int b(\mathbf{a}, R)\, W^2(\mathbf{a}, R)\, e^{j\varphi}\, d\Omega\, dr_I, \quad (3)$$

where

$$b(\mathbf{a}, R) = \int b(\mathbf{a}, R, f)\, df. \quad (4)$$

Note that $b(\mathbf{a}, R)$ is a frequency-averaged brightness spectrum as a function of three-dimensional location and will be termed the "brightness function." In many applications the cross spectrum $G(\mathbf{D}_i, k_m, \mathbf{D}_j, k_n, f)$ is used and can be obtained by a temporal Fourier transform of (1).

$$G(\mathbf{D}_i, k_m, \mathbf{D}_j, k_n, f) = \int b(\mathbf{a}, R, f)\, W^2(\mathbf{a}, R)\, e^{j\varphi}\, d\Omega\, dR. \quad (5)$$

It should be emphasized that (3) and (5) are the two fundamental equations of atmospheric radar imaging which express the relationship between the measurements (the correlation function at zero temporal lag or the cross spectrum) and the desired brightness estimates (the brightness function or the brightness spectrum). These two equations can be summarized in the following compressed notation:

$$V(\mathbf{D}_i, k_m, \mathbf{D}_j, k_n; f) = \int b(\mathbf{a}, R; f)\, W^2(\mathbf{a}, R)\, e^{j\varphi}\, d\Omega\, dR. \quad (6)$$

where $V(\mathbf{D}_i, k_m, \mathbf{D}_j, k_n; f)$ and $b(\mathbf{a}, R; f)$ are termed the "visibility function" and the "three-dimensional brightness distribution" (or simply the brightness distribution), respectively. In other words, the dependence of f on both sides of (6) only exists when the cross spectrum and the brightness spectrum are used. In this case, the brightness spectrum is solved independently for each frequency. This represents the so-called "Doppler sorting" property, which is extremely useful when no prior knowledge of how the atmospheric structure moves as a function of Doppler frequency is available. On the other hand, when the Doppler information is not needed, the correlation function at zero temporal lag is employed and the computational load becomes much smaller. From (6) it is shown that atmospheric radar imaging can be posed as an inverse problem given estimates of the visibility function. In practice, because of the difference in received power from various sensors the normalized visibility function should be used to estimate the brightness distribution, which has a unit of normalized power density [e.g., *Farley et al.*, 1981; E. Kudeki, unpublished lecture notes, 1995].

2.2. Special Case: Coherent Radar Imaging

CRI is designed to image the angular distribution of the reflectivity field by employing multiple spatially separated receivers but with only a single transmit frequency. Therefore the visibility function can be simplified as a function of spatial lag with the following form by setting $k_m = k_n = k$ in the exponent of (6). As a result,

$$V(\mathbf{l}; f) = \int b_a(\mathbf{a}; f)\, W_a^2(\mathbf{a})\, e^{jk\,\mathbf{a}\cdot\mathbf{l}}\, d\Omega, \quad (7)$$

where $b_a(\mathbf{a}; f)$ represents "angular brightness" because it reveals the angular distribution of the power density and is given by the following equation:

$$b_a(\mathbf{a}; f) = \int b(\mathbf{a}, R; f)\, W_r^2(R)\, dR. \quad (8)$$

Thus angular brightness is the range-averaged brightness distribution weighted by the square of the range-weighting function. It is evident from (7) that the angular brightness can be obtained by taking an inverse Fourier transform of the continuous visibility function and, subsequently, removing the effect of the antenna pattern.

2.3. Special Case: Range Imaging

In the RIM case, a single receiver but multiple frequencies are used. Furthermore, the receiver and transmitter are typically collocated at the origin. Therefore the visibility function can be simplified as a function of Δk by setting $\mathbf{D}_i = \mathbf{D}_j = \mathbf{0}$ in (6), resulting in the following form:

$$V(\Delta k;\, f) = \int b_r(R;\, f)\, W_r^2(R)\, e^{-j2\Delta k R}\, dR, \tag{9}$$

where the "range brightness" $b_r(R; f)$ is defined by the equation

$$b_r(R;f) = \int b(\mathbf{a}, R;f)\, W_a^2(\mathbf{a})\, d\Omega. \tag{10}$$

Therefore the range brightness is an angular averaged brightness weighted by the square of the antenna pattern. It is apparent that the range distribution of power density $b_r(r_I;\, f)W_r^2(R)$, which is also a Fourier transform of visibility function $V(\Delta k;f)$, can be estimated using a set of shifted transmit frequencies. If only two shifted transmit frequencies are used and $b_r(R; f)$ is assumed to have a Gaussian distribution, it can be shown from (9) that the mean and variance of $b_r(R; f)$ can be derived from the phase and magnitude of the visibility function, respectively. This is the well-known FDI technique, and it is necessary to note that the earlier FDI results proposed by *Kudeki and Stitt* [1987] can be reproduced by calculating the normalized correlation function at zero temporal lag in (9) without considering the range-weighting function. Moreover, (9) is a general formula without assumptions of the shape of the layer and the number of layers. However, the number of frequencies and their spacing have been shown to limit how well those layers can be reconstructed [*Palmer et al.*, 1999; *Yu*, 2000].

3. Estimation Algorithms

From (6), (7), and (9) it is evident that atmospheric radar imaging can be postulated as an inverse problem given an incomplete sampling of the visibility function calculated from signal pairs from shifted frequencies and/or spaced receivers. Two approaches are investigated in this work for 3-D imaging, which are the beam-forming technique, including the Fourier and Capon methods, and the MaxEnt method.

3.1. Beam-Forming Techniques

"Beam forming" is a term used in array signal processing which describes the process of focusing the sensitivity of a group of sensors in a specific direction [*Johnson and Dudgeon*, 1993]. In other words, beam forming is a means of combining the output from sensors to enhance SNR, locate the source of the signals, track signal sources, etc. Although the concept of beam forming is typically presented from the perspective of spatially separated sensors (i.e., CRI) [*Palmer et al.*, 1998], the same idea can be applied to RIM [*Palmer et al.*, 1999; *Luce et al.*, 2001] and 3-D imaging.

In order to derive a generalized representation of the beam-forming technique it is assumed that signals are from N spatially separated receivers located at $\mathbf{D}_1, \mathbf{D}_2, \ldots, \mathbf{D}_N$ and M closely spaced transmitter frequencies at $k_1, k_2, \ldots, k_M$. Let $\mathbf{s}(t)$ represent a column vector with size $N_t = NM$ containing the signals from these receivers and transmit frequencies. One way to construct $\mathbf{s}(t)$ is to let the first N components represent signals coming from all N receivers and the first transmit frequency, the second N components are from N receivers with the second transmit frequency, etc. Therefore $\mathbf{s}(t)$ can be represented in the following form:

$$\mathbf{s}(t) = \begin{bmatrix} s(\mathbf{D}_1,k_1,t) & s(\mathbf{D}_2,k_1,t) & \ldots & s(\mathbf{D}_N,k_1,t) \\ s(\mathbf{D}_1,k_2,t) & s(\mathbf{D}_2,k_2,t) & \ldots & s(\mathbf{D}_N,k_2,t) \\ \vdots & & & \\ s(\mathbf{D}_1,k_M,t) & s(\mathbf{D}_2,k_M,t) & \ldots & s(\mathbf{D}_N,k_M,t) \end{bmatrix}^T, \tag{11}$$

where T is the transpose operator. Note that the dependence of the signals on wave number and receiver location has been omitted from the left side of (11) for notational simplicity.

It can be shown that the brightness distribution is estimated by introducing a weighting vector $\mathbf{w}$ onto signals with the following form [e.g., *Palmer et al.*, 1998]:

$$\hat{b}(\mathbf{a}, R;f) = \frac{1}{W^2(\mathbf{a}, R)}\mathbf{w}^\dagger \mathbf{V}\mathbf{w} \tag{12}$$

where the dagger represents the Hermitian (conjugate transpose) operator and $\mathbf{V}$ is termed the visibility matrix with size $N_t \times N_t$ and is represented in the following form:

$$\mathbf{V} = \begin{bmatrix} V_{11} & V_{12} & \ldots & V_{1N_t} \\ V_{21} & V_{22} & \ldots & V_{2N_t} \\ \vdots & \vdots & \ddots & \vdots \\ V_{N_t1} & V_{N_t2} & \ldots & V_{N_tN_t} \end{bmatrix}, \tag{13}$$

where the element V_{pq} is the estimate of visibility function from the pth signals and the qth signals in (11). The corresponding indices of wave number k_n and receiver $\mathbf{D}_i$ for the pth signal can be determined

using $p = n\ N + i$. From (12) the brightness distribution can be estimated if the weighting vector is specified. Although various choices of the weighting vector can be employed based on the specific requirements, only the Fourier and Capon methods, which have been widely used in CRI and RIM, are presented here.

3.1.1. Fourier method. The goal of beam forming for the case of 3-D imaging is to introduce proper weights to signals from shifted frequencies and separated receivers to create constructive interference at a three-dimensional location where the brightness distribution is estimated. Signals from different receivers and wave numbers can be added coherently at the location of scatterer **R** by introducing weights which are selected to cancel the phase of the individual signals as shown in (26). This choice of the weighting vector has been used in CRI and RIM and is termed the Fourier method [*Palmer et al.*, 1998, 1999]. The weighting vector of Fourier3D shall be written in the following form according to (11):

$$\mathbf{w}_f = \begin{bmatrix} e^{j(2k_1R - k_1\mathbf{a}\cdot\mathbf{D}_1)} & e^{j(2k_1R - k_1\mathbf{a}\cdot\mathbf{D}_2)} & \cdots & e^{j(2k_1R - k_1\mathbf{a}\cdot\mathbf{D}_N)} \\ e^{j(2k_2R - k_2\mathbf{a}\cdot\mathbf{D}_1)} & e^{j(2k_2R - k_2\mathbf{a}\cdot\mathbf{D}_2)} & \cdots & e^{j(2k_2R - k_2\mathbf{a}\cdot\mathbf{D}_N)} \\ \vdots & & & \\ e^{j(2k_MR - k_M\mathbf{a}\cdot\mathbf{D}_1)} & e^{j(2k_MR - k_M\mathbf{a}\cdot\mathbf{D}_2)} & \cdots & e^{j(2k_MR - k_M\mathbf{a}\cdot\mathbf{D}_N)} \end{bmatrix}^T. \tag{14}$$

The Fourier brightness estimate is obtained by substituting (14) into (12). For the Fourier CRI method the weighting vector is simplified to the first N terms of (14) and is the same as the one proposed by *Palmer et al.* [1998] with a difference in sign convention. By taking every Nth weight in (14) the Fourier RIM weighting vector for M transmit frequencies [*Palmer et al.*, 1999] can be obtained. Characteristics and limitations of the Fourier method have been provided in the literature [*Palmer et al.*, 1998; *Yu et al.*, 2000].

3.1.2. Capon method. The Capon method has been proven to be robust and to provide enhanced resolution for the special cases of CRI and RIM [e.g., *Palmer et al.*, 1998, 1999; *Yu et al.*, 2000; *Chau and Woodman*, 2001]. By solving a constrained optimization problem an optimal weighting vector which adapts to suppress interference can be derived, resulting in the following form:

$$\mathbf{w}_c = \frac{\mathbf{V}^{-1}\mathbf{e}}{\mathbf{e}^\dagger\mathbf{V}^{-1}\mathbf{e}}, \tag{15}$$

where the steering vector is denoted by **e** and has the same form as (14) for 3-D imaging. As a result, the brightness distribution estimated using Capon3D is presented by the following equation:

$$\hat{b}_c(\mathbf{a}, R; f) = \frac{1}{W^2(\mathbf{a}, R)} \frac{1}{\mathbf{e}^\dagger\mathbf{V}^{-1}\mathbf{e}}. \tag{16}$$

A detailed derivation is given by *Palmer et al.* [1998]. It should be noted that the special cases of Capon CRI and RIM are identical to (16) with the exception of the steering vector **e**.

3.2. Maximum Entropy Method

The MaxEnt method was developed to solve an ill-conditioned problem where data are incomplete and noisy [*Gull and Daniell*, 1978]. For studies of atmospheric radar imaging, the visibility function can be estimated only for certain lags because a finite number of receivers and transmit frequencies are used. Thus the data are incomplete. Furthermore, signals are inevitably corrupted by various types of noise such as system noise and cosmic noise. Therefore the MaxEnt method is ideally suitable to solve the inverse problem posed in (6) [e.g., *Hysell*, 1996; *Hysell and Woodman*, 1997], which attempts to reconstruct the distribution of the reflectivity field within a resolution volume given incomplete and noisy visibility data.

Mathematically, MaxEnt3D is stated as a constrained optimization problem described by the following equations:

$$\max_b \ \mathrm{H}_2 \quad \text{subject to}$$

$$\sum_{\mathbf{R}} b(\mathbf{a}, R; f)\, \mathrm{W}^2(\mathbf{a}, R) = F, \tag{17}$$

$$V_q(\mathbf{D}_i, k_m, \mathbf{D}_j, k_n; f) + e_q = \sum_{\mathbf{R}} b(\mathbf{a}, R; f)\, W^2(\mathbf{a}, R)\, h_q(\mathbf{a}, R) \tag{18}$$

$$q = 1, 2, \ldots, N_v,$$

$$\sum_{q=1}^{N_v} \frac{e_q^2}{\sigma_q^2} = \Lambda, \tag{19}$$

where the number of visibility measurements is denoted by N_v and H_2 is the so-called entropy and is described by the equation

$$H_2 = -\sum_{\mathbf{R}} b(\mathbf{a}, R;\ f)\ \ln b(\mathbf{a}, R;\ f). \tag{20}$$

The summation with respect to **R** in (17), (18), and (20) is performed over the three-dimensional space where the brightness distribution $b(\mathbf{a},R;f)$ is estimated and is typically limited by the resolution volume. The first constraint, equation (17), restricts the sum of the

brightness distribution to a finite value (F) in order to obtain a valid amplitude estimation. The second constraint provides the relationship between the brightness distribution and visibility function in a discrete form of (6) allowing an unknown measurement error e_q. Additionally, $h_q(\mathbf{a}, R)$ is defined by the following equations and can be either a sine or cosine function depending on whether the imaginary or real part of $V_q(\mathbf{D}_i, k_m, \mathbf{D}_j, k_n; f)$ is used, respectively.

$$h_q(\mathbf{a}, R) = \begin{cases} \cos(\varphi) & \Re\{V_q(\mathbf{D}_i, k_m, \mathbf{D}_j, k_n; f)\} \\ \sin(\varphi) & \Im\{V_q(\mathbf{D}_i, k_m, \mathbf{D}_j, k_n; f)\} \end{cases}, \tag{21}$$

where φ is defined in (2) and $\Re\{\ \}$ and $\Im\{\ \}$ denote the real and imaginary parts of the argument, respectively. The last constraint, equation (19), is an expression of errors. It is assumed that these measurement errors e_q are uncorrelated, independent, and Gaussian-distributed with zero mean and standard deviation σ_q. As a result, the summation of error has a χ^2 distribution with mean Λ [e.g., *Cooper and McGillem*, 1986]. This error constraint was introduced by *Gull and Daniell* [1978], and the value of Λ is typically set equal to the number of visibility measurements N_v.

The MaxEnt solution can be derived using Lagrange methods [*Luenberger*, 1984], and a model of the brightness distribution can be obtained in terms of Lagrange multipliers λ_i.

$$\hat{b}_m(\mathbf{a}, R; f) = \frac{F}{W^2(\mathbf{a}, R)\, Z} \exp\left[-\sum_{i=1}^{N_v} \lambda_i h_i(\mathbf{a}, R)\right], \tag{22}$$

where

$$Z = \sum_{\mathbf{R}} \exp\left[-\sum_{i=1}^{N_v} \lambda_i h_i(\mathbf{a}, R)\right]. \tag{23}$$

Note that the model described in (22) and (23) is suitable for both CRI and RIM with only slight modifications, which are now described. First, the argument of sin and cos in (21) is simplified to be either $k\mathbf{a} \cdot \mathbf{l}$ or $-2\Delta kR$ according to (7) and (9) for CRI and RIM, respectively. Second, because only the angular or range distribution of the brightness distribution is estimated for CRI and RIM, the summation of $\mathbf{R}$ in (17), (18), and (20) is performed in the direction of only angle $\mathbf{a}$ or range R.

4. Simulation Results

The simulation model used in this work was developed by *Holdsworth and Reid* [1995] and has been successfully applied to studies of atmospheric radar imaging by *Palmer et al.* [1999] and *Yu et al.* [2000]. By allowing a field of scatterers to advect through an enclosing volume which is weighted by atmospheric reflectivity, the antenna pattern, and the range-weighting function, it is possible to study the potential of atmospheric radar imaging to reconstruct atmospheric structure in angle and/or range. A set of time series data for a specific receiver and transmit frequency is obtained by coherently summing the complex signals of each individual scatterer. The position of each scatterer is updated by a mean wind and spatially correlated turbulent motion at each sampling time. A white, Gaussian, and properly scaled complex noise sequence can be added to the time series to produce the desired SNR.

In this work, the radar volume is centered at 10.0 km with a size defined by a 1 μs transmit pulse and a 3.6° half-power beam width. A total of 200 scatterers are advected through the enclosing volume by a mean westerly wind of 30 ms^{-1} and a three-dimensional turbulent motion of 0.5 ms^{-1}. The sampling time of 0.1 s includes the coherent integration time with each record containing 256 data points (25.6 s). In order to demonstrate the feasibility of 3-D imaging, signals from four receivers and three frequencies were generated simultaneously. The receiver configuration is the same as configuration II proposed by *Yu et al.* [2000]. One of the receivers was collocated with the transmitter at the origin, and the other three receivers were located 39.2 m from the center with azimuth angles of 96.58°, 216.58°, and 336.58°. The three transmit frequencies were selected to have nonredundant spacing at 49.50 MHz, 49.83 MHz, and 50.50 MHz in order to improve the estimates [*Johnson and Dudgeon*, 1993].

The modeled atmospheric reflectivity is described by two blob-like scattering regions with sizes smaller than the radar volume in both angular and range in order to test the capability of 3-D imaging. Each scattering region is modeled by a Gaussian distribution with a three-dimensional mean location and variance. The units used in the horizontal (zonal and meridional) and vertical directions are degrees and meters, respectively. Initially, these two localized scattering regions were centered at (−0.54°, 3.25°, 10.043 km) and (−1.36°, −2.6°, 9.957 km), both with widths of 7 m in range and 1° in angle as shown in the leftmost plot of Figure 2a.

Subsequently, their locations were changed to become closer in both angle and range at intervals of five records, which is also the number of incoherent integrations used for the visibility measurements. It should be pointed out that in reality, the estimated brightness distribution could

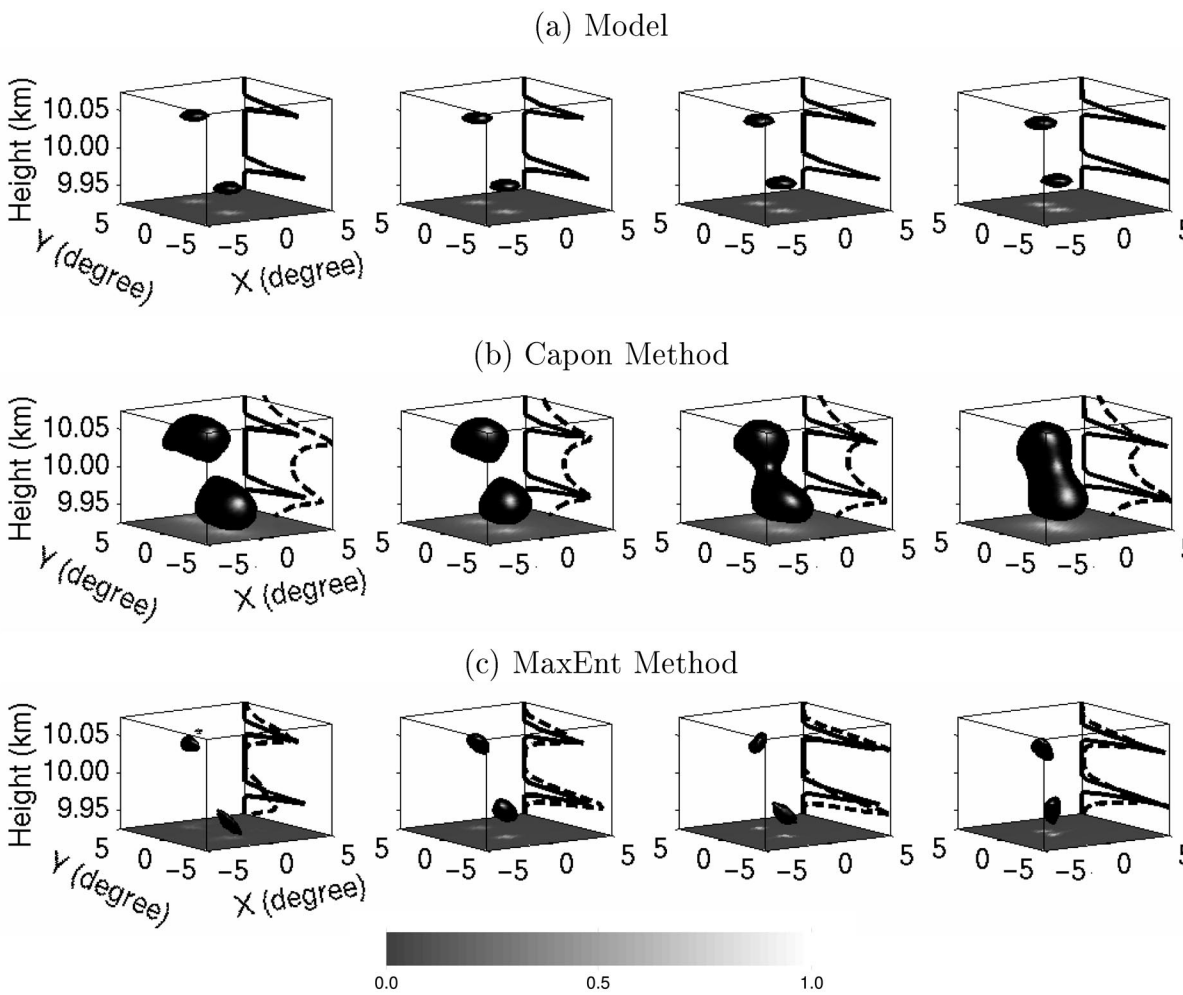

Figure 2. (a) Model brightness and results of 3-D imaging using the (b) Capon and (c) MaxEnt methods for an SNR of 20 dB. In Figure 2a, two simulated patches are moving toward each other from left to right as time evolves. The brightness functions were estimated at a $32 \times 32 \times 32$ uniform grid using four receivers and three frequencies. It is evident that Capon3D and MaxEnt3D can track and distinguish the two patches.

be smeared in position because of the effect of finite integration on continuously moving targets. However, the main purpose of this simulation is to study the sensitivity of the algorithms to various SNR. Therefore each sequence in Figure 2a can be considered as an independent case where the overall structure is stationary. The resolution capability will be tested when the two scattering regions are close.

The visibility function was calculated using the normalized correlation function at zero temporal lag, and the brightness function was estimated on a $32 \times 32 \times 32$ uniform grid within $\pm 5^\circ$ in both the zonal and meridional directions and 150 m in the vertical direction. In addition, brightness estimates were normalized to their maximum value of the four frames. Results from Capon3D and MaxEnt3D for an SNR of 20 dB are shown in Figures 2b and 2c, respectively. The two black patches in Figure 2 indicate an isosurface of model weighting or the brightness estimates including range-weighting and antenna pattern effects at a value of 0.06 of the maximum value. The model and associated angular brightness estimates, which were calculated using (8), are shown on the bottom of each plot, respectively. The model range distribution and results from (10) are denoted by the solid lines and dashed lines, respectively. It is evident that Capon3D and

MaxEnt3D can clearly distinguish the two scattering regions in both angle and range. An exception is noted for Capon3D in the case of the smallest separation. In all cases, however, the widths of structures are overestimated using Capon3D. Moreover, Fourier3D produced much broader structures than Capon3D did and can barely distinguish two scattering regions only in the case of the largest separation. Therefore it is difficult to present in the same scale, and no qualitative results of Fourier3D are shown. It has to be mentioned that the results of 3-D imaging can be improved by properly adding more receivers and transmit frequencies to cover a wider range of spatial lags and frequency spacing. Statistical comparisons of resolution using various receiver configurations and frequency sampling for special cases of CRI and RIM were made by *Yu et al.* [2000] and *Palmer et al.* [1999], respectively. Here, the focus is on demonstrating the feasibility of 3-D imaging using a minimal configuration.

The effect of noise upon three-dimensional brightness estimates is the same as for CRI and RIM, exemplified by a broadening of the estimated structure with decreasing SNR. Performance of Fourier3D, Capon3D, and MaxEnt3D was measured by calculating the mean-square error (MSE) between the three-dimensional model and reconstructed images on a pixel-by-pixel basis as demonstrated by *Palmer et al.* [1999] and *Yu* [2000]. Statistical comparisons were made by calculating the sample mean of MSE for various SNR and are shown in Figure 3.

Each data point represents the mean MSE of 20 realizations of the additive noise sequence while the total length of the error bars indicates 4 times the standard deviation of the MSE. Note that the error bars of the Capon and MaxEnt methods for high SNR are too small to be identified. From Figure 3 it is evident that MaxEnt3D outperforms the other two methods for all SNR values while Capon3D approaches the MaxEnt3D results for high SNR. The performance of Fourier3D is limited by resolution, resulting in relatively high MSE values. Similar comparisons were reported for the special cases of CRI [*Yu et al.*, 2000; *Chau and Woodman*, 2001] and RIM [*Yu*, 2000]. It should be mentioned that the background noise component was subtracted form the visibility measurements for the Fourier and MaxEnt methods. As emphasized by *Hysell* [1996], such a procedure is the most important factor in the MaxEnt method, which avoids the MaxEnt solution from reverting to the Fourier method. Note that MSE values of Fourier3D without subtracting background noise were also calculated and, as expected, showed a similar dependence of SNR to Capon3D with a mean MSE value of approximately 0.24 for SNR = −5 dB. In other words, the noise removal algorithm used for the Fourier method can mitigate the contamination of uncorrelated noise existing in the time series data to maintain an approximately constant performance even for an SNR as low as −5 dB. In limited cases, however, this noise removal procedure was observed to cause the visibility matrix to become singular, and the Capon method did not produce reliable images. In order to compare the best performance of each technique as shown in Figure 3, subtraction of background noise component was implemented for Fourier3D and MaxEnt3D but not for Capon3D. The noise component was estimated by applying a polynomial-fitting algorithm on the autocorrelation function about the zero temporal lag.

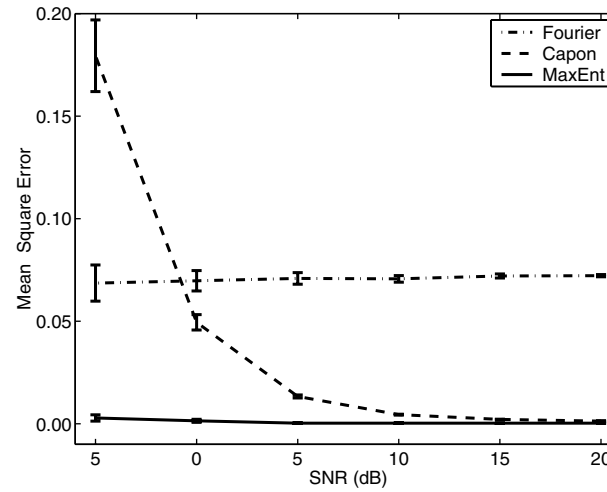

Figure 3. Statistical comparisons of Fourier3D, Capon3D, and MaxEnt3D for SNR from −5 dB to 20 dB sampled every 5 dB. Each data point represents a mean MSE of 20 realizations, and the error bars indicate 4 times the standard deviation. The MaxEnt method has superior performance for all SNR values with the lowest MSE values. The Capon3D performance approaches the MaxEnt3D performance for relatively high SNR.

5. Conclusions

One of the goals for this work was to develop a generalized formulation between the CRI and RIM, combining the advantages of both multiple-receiver and multiple-frequency techniques. A model was established to express the relationship between the desired three-dimensional brightness estimates and the visibility measurements of signals from spaced receivers and

shifted frequencies. For the first time, this theory provided the mathematical foundation of 3-D imaging. Although many algorithms can be used to solve for the brightness estimates, only the Fourier, Capon, and MaxEnt methods were investigated in this study. The idea of Fourier3D, Capon3D, and MaxEnt3D is similar to special cases of CRI and RIM but in a more general manner, in which the three-dimensional brightness is desired. Special cases of CRI and RIM for the three methods proposed in earlier work can be obtained by properly modifying the general 3-D imaging representation.

In order to further study atmospheric radar imaging, a numerical model with properly designed weighting functions was used to validate and exercise these techniques. It was qualitatively shown that atmospheric reflectivity could be reconstructed using Capon3D and MaxEnt3D for the case of four receivers and three frequencies. It is expected that Fourier3D can produce similar performance to that of Capon3D or MaxEnt3D using more receivers and transmit frequencies. However, such an equivalent configuration cannot be determined in general because of the adaptive nature of the Capon and MaxEnt methods. A quantitative measure of performance was made by calculating the MSE between the model reflectivity and estimated brightness. As expected, the results showed that the MaxEnt3D and Capon3D techniques had similar performance for the high-SNR case. However, cases with low SNR proved to be more accurately reconstructed using the MaxEnt method.

Appendix A: Derivation of the Cross-Correlation Function

The coherently detected, baseband signals of k_m wave number at the ith receiver as shown in Figure 1, $s(\mathbf{D}_i, k_m, t)$, are given by the following equation under the far-field assumption [e.g., *Liu and Pan*, 1993; *Doviak et al.*, 1996]:

$$s(\mathbf{D}_i, k_m, t) = \int \frac{E(\mathbf{a}, R, t)\, W(\mathbf{a}, R)}{R r_i}\, e^{-jk_m(R+r_i)}\, dV, \qquad (24)$$

where $E(\mathbf{a}, R, t)$ represents both fluctuations in the refractive index and a weighting function specifying where these fluctuations occur [e.g., *Luce et al.*, 2000] and the weighting function of the radar system is indicated by $W(\mathbf{a}, R)$ including the antenna pattern $W_a(\mathbf{a})$ and range-weighting function $W_r(R)$ [e.g., *Doviak et al.*, 1996]. Moreover, both $E(\mathbf{a}, R, t)$ and $W(\mathbf{a}, R)$ are represented as a function of range R and angular location $\mathbf{a}$ for the sake of discussions of special cases of CRI and RIM. Note that $\mathbf{a}$ is a unit vector, $\mathbf{a} = \mathbf{R}/R$, and can be represented as a function of angular location $\mathbf{a} = [\sin\theta \sin\phi \quad \sin\theta \cos\phi \quad \cos\theta]$, where the zenith and azimuth angles are denoted by θ and ϕ, respectively.

The distance r_i can be approximated by $R - \mathbf{a} \cdot \mathbf{D}_i$ by retaining only the first-order term in a Taylor series expansion given that the following condition is satisfied:

$$D_{max} \ll \sqrt{\frac{R\lambda}{\pi}}, \qquad (25)$$

where $D_{\max}$ is the maximum distance between transmitter and receivers and λ is the radar wavelength. For example, $D_{\max}$ should be shorter than approximately 138 m to image the atmospheric structure within a resolution volume centered at 10 km for a 50 MHz radar, which is typically true. Therefore (24) can be approximated by the following equation:

$$s(\mathbf{D}_i, k_m, t) \cong \int E(\mathbf{a}, R, t)\, W(\mathbf{a}, R)\, e^{j(-2k_m R + k_m \mathbf{a}\cdot\mathbf{D}_i)}\, dR\, d\Omega, \qquad (26)$$

where Ω is the solid angle. Following the same manner, signals of wave number k_n at the jth receiver can also be derived. Under the wide sense stationary assumption, the correlation function between these two signals is defined by the following equation:

$$R(\mathbf{D}_i, k_m, \mathbf{D}_j, k_n, \tau) = \langle s^*(\mathbf{D}_i, k_m, t) s(\mathbf{D}_j, k_n, t+\tau)\rangle, \qquad (27)$$

where the asterisk is the complex conjugate operator and the angle brackets are the expected value operator. When the scattering region is highly localized, the complex amplitude of $E(\mathbf{a}, R, t)$ at $\mathbf{R}$ can be assumed to be an independent, zero-mean random variable. As a result, the complex amplitudes from distinct location $\mathbf{R}$ and $\mathbf{R}'$ are uncorrelated, and (27) can be simplified in the following form:

$$R(\mathbf{D}_i, k_m, \mathbf{D}_j, k_n, \tau) = \int b(\mathbf{a}, R, f)\, W^2(\mathbf{a}, R)\, e^{j2\pi f\tau}\, e^{j\varphi} d\Omega\, dR\, df, \qquad (28)$$

$$\varphi = -2\Delta k\, R + k_m \mathbf{a}\cdot\mathbf{l} + \Delta k\, \mathbf{a}\cdot\mathbf{D}_j, \qquad (29)$$

where the spatial lag and wave number difference are defined by $\mathbf{l} = \mathbf{D}_j - \mathbf{D}_i$ and $\Delta k = k_n - k_m$, respectively. Additionally, the brightness spectrum is defined by the following equation as a function of three-dimensional location and Doppler frequency f:

$$b(\mathbf{a}, R, f) = \langle |E(\mathbf{a}, R, f)|^2 \rangle. \qquad (30)$$

From (30) it is noted that the brightness spectrum must be nonnegative because it is a measure of power density. For the case of volume scattering, the brightness spectrum has a more general form with a dependence of $\mathbf{R}' - \mathbf{R}$ and can be further represented in terms of the turbulence spatial spectrum and wind velocity [e.g., *Liu and Pan*, 1993; *Doviak et al.*, 1996]. In such a case, the brightness spectrum can be thought of as a uniformly distributed function within the resolution volume. As a result, the weighting function of the radar system is reconstructed using imaging techniques. However, further theoretical work or experimental results are needed to verify this hypothesis.

Acknowledgments. R.D.P. and T.-Y.Y. were supported by the Division of Atmospheric Sciences of the National Science Foundation through grant ATM 99-08616. R.D.P. was also supported by the Army Research Office through grant DAAD-19-01-10407.

References

Capon, J., High-resolution frequency-wavenumber spectrum analysis, *Proc. IEEE*, *57*, 1408–1419, 1969.

Chau, J. L., and R. F. Woodman, Three-dimensional coherent radar imaging at Jicamarca: Comparison of different inversion techniques, *J. Atmos. Sol.-Terr. Phys.*, *63*, 253–261, 2001.

Chilson, P. B., and G. Schmidt, Implementation of frequency domain interferometry at the SOUSY VHF radar: First results, *Radio Sci.*, *31*, 263–272, 1996.

Chilson, P. B., R .D. Palmer, A. Muschinski, D. Hooper, G. Schmidt, and H. Steinhagen, SOMARE-99: A demonstrational field campaign for ultra-high resolution VHF atmospheric profiling using frequency diversity, *Radio Sci.*, *36*, 695–707, 2001.

Cooper, G. R., and C. D. McGillem, *Probabilistic Methods of Signal and System Analysis*, Oxford Univ. Press, New York, 1986.

Doviak, R. J., R. J. Lataitis, and C. L. Holloway, Cross-correlation and cross-spectra in spaced-antenna wind profilers, 1, Theoretical analysis, *Radio Sci.*, *31*, 157–180, 1996.

Farley, D., H. Ierkic, and B. Fejer, Radar interferometry: A new technique for studying plasma turbulence in the ionosphere, *J. Geophys. Res.*, *86*, 1467–1472, 1981.

Franke, S. J., Pulse compression and frequency domain interferometry with a frequency-hopped MST radar, *Radio Sci.*, *25*, 565–574, 1990.

Gull, S. F., and G. J. Daniell, Image reconstruction from incomplete and noisy data, *Nature*, *272*, 686–690, 1978.

Haykin, S., J. H. Justice, N. L. Owsley, J. Y. Yen, and A. C. Kak, *Array Signal Processing*, Prentice-Hall, Old Tappan, N. J., 1985.

Hélal, D., M. Crochet, H. Luce, and E. Spano, Radar imaging and high-resolution array processing applied to a classical VHF-ST profiler, *J. Atmos. Sol.-Terr. Phys.*, *63*, 263–274, 2001.

Holdsworth, D. A., and I. M. Reid, A simple model of atmospheric radar backscatter: Description and application to the full correlation analysis of spaced antenna data, *Radio Sci.*, *30*, 1263–1280, 1995.

Hysell, D. L., Radar imaging of equatorial *F* region irregularities with maximum entropy interferometry, *Radio Sci.*, *31*, 1567–1578, 1996.

Hysell, D. L., and R. F. Woodman, Imaging coherent backscatter radar observations of topside equatorial spread *F*, *Radio Sci.*, *32*, 2309–2320, 1997.

Johnson, D. H., and D. E. Dudgeon, *Array Signal Processing*, Prentice-Hall, Old Tappan, N. J., 1993.

Kudeki, E., and G. R. Stitt, Frequency domain interferometry: A high-resolution radar technique for studies of atmospheric turbulence, *Geophys. Res. Lett.*, *14*, 198–201, 1987.

Kudeki, E., and F. Sürücü, Radar interferometric imaging of field-aligned plasma irregularities in the equatorial electrojet, *Geophys. Res. Lett.*, *18*, 41–44, 1991.

Kudeki, E., and R. Woodman, A poststatistics steering technique for MST radar applications, *Radio Sci.*, *25*, 591–594, 1990.

Liu, C. H., and C. J. Pan, New observational techniques for studying the dynamics of the middle atmosphere using the Chung Li VHF radar, *J. Atmos. Terr. Phys.*, *55*, 1055–1066, 1993.

Luce, H., J. Röttger, M. Yamamoto, and S. Fukao, Scattering layer thickness and position estimated by radar frequency domain interferometry, 1, Effects of the limited horizontal extent and advection of the scattering layers, *Radio Sci.*, *35*, 119–131, 2000.

Luce, H., M. Yamamoto, S. Fukao, D. Helal, and M. Crochet, A frequency domain radar interferometric imaging (FII) technique based on high resolution methods, *J. Atmos. Sol.-Terr. Phys.*, *63*, 221–234, 2001.

Luenberger, D. G., *Linear and Nonlinear Programming*, Addison-Wesley-Longman, Reading, Mass., 1984.

Palmer, R. D., K. Y. Lei, S. Fukao, M. Yamamoto, and T. Nakamura, Weighted imaging Doppler interferometry, *Radio Sci.*, *30*, 1787–1801, 1995.

Palmer, R. D., S. Gopalam, T.-Y. Yu, and S. Fukao, Coherent radar imaging using Capon's method, *Radio Sci.*, *33*, 1585–1598, 1998.

Palmer, R. D., T.-Y. Yu, and P. B. Chilson, Range imaging using frequency diversity, *Radio Sci.*, *34*, 1485–1496, 1999.

Palmer, R. D., P. B. Chilson, A. Muschinski, G. Schmidt, T.-Y. Yu, and H. Steinhagen, SOMARE-99: Observations of tropospheric scattering layers using multiple-frequency range imaging, *Radio Sci.*, *36*, 681–693, 2001.

Pfister, W., The wave-like nature of inhomogeneities in the *E*-region, *J. Atmos. Terr. Phys.*, *33*, 999–1025, 1971.

Röttger, J., and H. Ierkic, Postset beam steering and interferometer applications of VHF radars to study winds, waves, and turbulence in the lower and middle atmosphere, *Radio Sci.*, *20*, 1461–1480, 1985.

Röttger, J., and R. A. Vincent, VHF radar studies of tropospheric velocities and irregularities using spaced antenna techniques, *Geophys. Res. Lett.*, *5*, 917–920, 1978.

Woodman, R. F., Inclination of the geomagnetic field measured by an incoherent scatter technique, *J. Geophys. Res.*, *76*, 178–184, 1971.

Woodman, R. F., Coherent radar imaging: Signal processing and statistical properties, *Radio Sci.*, *32*, 2372–2391, 1997.

Yu, T.-Y., Radar study of the atmosphere using spatial and frequency diversity, Ph.D. dissertation, Univ. of Nebr., Lincoln, 2000.

Yu, T.-Y., R. D. Palmer, and D. L. Hysell, A simulation study of coherent radar imaging, *Radio Sci.*, *35*, 1129–1141, 2000.

R. D. Palmer, Department of Electrical Engineering, University of Nebraska, 209N Walter Scott Engineering Center, 17th and Vine Streets, Lincoln, NE 68588-0511, USA. (bpalmer@unl.edu)

T.-Y. Yu, Atmospheric Technology Division, National Center for Atmospheric Research, 3450 Mitchell Lane, Boulder, CO 80301-2260, USA. (tianyou@atd.ucar.edu)

(Received February 27, 2001; revised July 23, 2001;
accepted July 30, 2001.)